NeuroImage: Clinical 40 (2023) 103519

Contents lists available at ScienceDirect

NeuroImage: Clinical

journal homepage: www.elsevier.com/locate/ynicl

Subregional analysis of striatum iron in Parkinson's disease and rapid eye movement sleep behaviour disorder

Erind Alushaj [a,b], Dimuthu Hemachandra [c,d], Alan Kuurstra [c,e], Ravi S. Menon [c,e], Hooman Ganjavi [f], Manas Sharma [g,h], Alia Kashgari [i], Jennifer Barr [f], William Reisman [i], Ali R. Khan [c,e], Penny A. MacDonald [b,h,*]

[a] Department of Neuroscience, Schulich School of Medicine and Dentistry, Western University, London, Ontario, Canada
[b] Western Institute for Neuroscience, Western University, London, Ontario, Canada
[c] Robarts Research Institute, Western University, London, Ontario, Canada
[d] School of Biomedical Engineering, Western University, London, Ontario, Canada
[e] Department of Medical Biophysics, Western University, London, Ontario, Canada
[f] Department of Psychiatry, Western University, London, Ontario, Canada
[g] Department of Radiology, Western University, London, Ontario, Canada
[h] Department of Clinical Neurological Sciences, Western University, London, Ontario, Canada
[i] Department of Medicine, Respirology Division, Western University, London, Ontario, Canada

ARTICLE INFO

Keywords:
Parkinson's disease
Rapid eye movement sleep behaviour disorder
Quantitative susceptibility mapping
Striatum
Tractography

ABSTRACT

The loss of dopamine in the striatum underlies motor symptoms of Parkinson's disease (PD). Rapid eye movement sleep behaviour disorder (RBD) is considered prodromal PD and has shown similar neural changes in the striatum. Alterations in brain iron suggest neurodegeneration; however, the literature on striatal iron has been inconsistent in PD and scant in RBD.

Toward clarifying pathophysiological changes in PD and RBD, and uncovering possible biomarkers, we imaged 26 early-stage PD patients, 16 RBD patients, and 39 age-matched healthy controls with 3 T MRI. We compared mean susceptibility using quantitative susceptibility mapping (QSM) in the standard striatum (caudate, putamen, and nucleus accumbens) and tractography-parcellated striatum. Diffusion MRI permitted parcellation of the striatum into seven subregions based on the cortical areas of maximal connectivity from the Tziortzi atlas.

No significant differences in mean susceptibility were found in the standard striatum anatomy. For the parcellated striatum, the caudal motor subregion, the most affected region in PD, showed lower iron levels compared to healthy controls. Receiver operating characteristic curves using mean susceptibility in the caudal motor striatum showed a good diagnostic accuracy of 0.80 when classifying early-stage PD from healthy controls.

This study highlights that tractography-based parcellation of the striatum could enhance sensitivity to changes in iron levels, which have not been consistent in the PD literature. The decreased caudal motor striatum iron was sufficiently sensitive to PD, but not RBD. QSM in the striatum could contribute to development of a multivariate or multimodal biomarker of early-stage PD, but further work in larger datasets is needed to confirm its utility in prodromal groups.

1. Introduction

Parkinson's disease (PD) is the second most common and fastest-growing neurodegenerative disease in the world (Dorsey et al., 2018). PD is characterized by both motor (e.g., bradykinesia, tremor, rigidity, etc.) and non-motor symptoms (Barone et al., 2009). There are no objective tests to diagnose PD in clinical practice and no disease-modifying therapies or cures for the disease (Emre et al., 2014; Mitchell et al., 2021). Accurate diagnostic tests would improve clinical management and advance discovery of disease-modifying therapies for PD.

Clinical populations at increased risk for developing PD provide an opportunity to investigate neural changes that precede and lead to PD symptoms as well as to uncover preclinical biomarkers signalling who will convert to PD and over what period (Barber et al., 2017; Postuma

* Corresponding author.
E-mail address: penny.macdonald@gmail.com (P.A. MacDonald).

https://doi.org/10.1016/j.nicl.2023.103519
Received 12 July 2023; Received in revised form 24 September 2023; Accepted 26 September 2023
Available online 28 September 2023

et al., 2012). Rapid eye movement sleep behaviour disorder (RBD) is a substantial risk factor for PD and other alpha-synucleinopathies such as multiple system atrophy (MSA) and Lewy body dementia (LBD; Schenck et al., 2019). A recent study identified alpha-synuclein seeds in the cerebrospinal fluid of RBD patients (Concha-Marambio et al., 2023). RBD requires objective v ideo polysomnography for confirmation, which identifies electromyographic abnormalities during REM sleep (American Academy of Sleep Medicine, 2014). This lack of normal muscular paralysis during REM sleep can lead to dream-enactment behaviour, which is a main diagnostic criterion of RBD (American Academy of Sleep Medicine, 2014).

Emerging evidence from several groups has suggested up to 75% of RBD patients will develop an alpha-synucleinopathy, suggesting RBD is one of the strongest predictors of neurodegeneration (Iranzo et al., 2014; Postuma et al., 2019; Postuma and Berg, 2016; Schenck et al., 2013). In a large multi-centre study, of the RBD patients who phenoconverted, 52% developed PD, 4% developed MSA, and 44% developed LBD (Postuma et al., 2019). RBD generally exists for years before parkinsonian motor symptom onset, which heralds a diagnosis of PD (Hogl et al., 2018). Discovery of preclinical biomarkers could promote earlier diagnosis, provide targets for treatment, and improve the health of over ten million PD patients worldwide (Lehericy et al., 2017).

Degeneration of the nigrostriatal pathway, which connects the dopamine-producing neurons of the substantia nigra pars compacta (SNc) and the striatum, is widely accepted as the main contributor to motor deficits in PD (Peran et al., 2010; Prasad et al., 2018). Up to 80% of nigral dopaminergic neurons will have degenerated by the timepoint of clinical diagnosis of PD (Cheng et al., 2010). Iron elevation in the SNc is a consistent feature of PD, which might contribute to or signal neurodegeneration in dopaminergic neurons (Ayton & Lei, 2014). In this way, abnormal iron deposition might serve as a tool for understanding RBD and PD pathophysiology. Although iron is involved in cellular homeostasis, it is also implicated in neurodegeneration (Pyatigorskaya et al., 2020). There is substantial evidence to suggest that oxidative stress derived from iron and dopamine interactions contribute to neuronal loss and pathophysiology in PD (Cao and Dixon, 2016; Dixon et al., 2012; Hare and Double, 2016). It is unknown if iron accumulation is an initiator of neurodegeneration or a secondary event, nevertheless, iron overload is a potential marker of the PD state (Ayton & Lei, 2014). The properties of iron, its presence in the subcortical structures, its involvement in oxidative stress and neurodegeneration, as well as findings of elevated iron in PD, make it an ideal candidate for detecting and tracking PD longitudinally (Ayton & Lei, 2014), perhaps even from its preclinical/prodromal period.

Changes to striatal iron levels as measured by QSM have been reported less consistently than alterations to iron levels in the SNc in a recent systematic review (Ravanfar et al., 2021). The review found that overall, there was a non-significant trend towards *lower* susceptibility in the basal ganglia, which included the caudate nuclei, putamen, and GP, in PD patients relative to HCs (Ravanfar et al., 2021). In the caudate, nine of 18 studies trended toward lower iron levels, one showed increased caudal iron, and eight found no differences between PD patients and HCs (Ravanfar et al., 2021). In the putamen, nine of 22 studies trended toward lower iron levels, four revealed increased iron, and nine studies found no differences in putaminal iron levels between PD patients and HCs (Ravanfar et al., 2021). In the GP, eight out of 21 studies trended toward lower iron levels, while six revealed increased iron, and seven studies found no differences between PD patients and HCs (Ravanfar et al., 2021). Differences across patient samples and methodological approaches to region definition or QSM image generation could be contributing factors to the lack of consistency in this literature. Furthermore, the striatum is not as iron-rich as the SN or GP but might still provide neuroimaging features of PD for classification (Hallgren and Sourander, 1958). Given the importance of the striatum in the pathophysiology of PD, evaluating changes in iron is warranted toward understanding the disease and identifying biomarkers.

The first study of striatal iron in RBD found no differences between patients and HCs in the caudate or putamen when using R2* relaxometry (Lee et al., 2014). This technique has proven to be a less sensitive measure than QSM with regards to detecting nigral iron elevation due to PD, as QSM does a better job of accounting for local tissue susceptibility than R2* (Alushaj, 2019; Langkammer et al., 2016). Follow-up work using QSM, however, found no differences between RBD and HC, but reported marginally lower ($p = 0.058$) right putaminal mean susceptibility in PD compared to RBD patients (Sun et al., 2020). This finding was not replicated in a follow up study (Zhang et al., 2021). In fact, the most recent work only reported lower volume in the right caudate of RBD patients versus HCs, with no group differences in overall striatal susceptibility (Zhang et al., 2021).

Our aim in this study was to use QSM to investigate changes to striatal iron in patients with PD and RBD. Based on the results of the recent systematic review (Ravanfar et al., 2021), if changes occur in early-stage PD patients, mean susceptibility should be lower for this group in the striatum compared to HCs, suggesting lower iron levels. However, comparisons of iron measures extracted from standard striatal structures, such as the caudate nucleus, putamen, and nucleus accumbens often failed to reveal group differences between PD patients and HCs (Du et al., 2016; Ravanfar et al., 2021; Sethi et al., 2019; Takahashi et al., 2018), as well as between RBD patients and HCs (Sun et al., 2020; Zhang et al., 2021). In contrast to this previous work, we planned to measure iron in these standard striatal structures as well as in distinct functional subregions of the striatum. These striatal subregions are achieved using a parcellation technique developed in our lab (Khan et al., 2019). This approach relies on structural connectivity of the striatum to cortical regions, premised on work illustrating functional heterogeneity of these striatal subregions (Khan et al., 2019; Tziortzi et al., 2014). This parcellation approach generates seven subregions of the striatum. Voxels are classified based on the cortical region from the Tzortzi atlas to which they connect maximally. Susceptibility values from striatal subregions will be compared across early-staged PD patients, RBD patients, and HCs. The caudal motor subregion of the striatum is the earliest and most dopamine-deficient subregion in PD (Kish et al., 1988). We predict that combining QSM and this tractography-based parcellation will improve sensitivity to detect group differences, by enabling more targeted measures of the most affected regions in PD, and potentially in RBD, a precursor condition. These more sensitive measures might show potential to distinguish patients at the single-subject level, or to contribute to multivariate diagnostic biomarkers of PD or RBD.

2. Materials & methods

2.1. Participants

Twenty-six patients with early-stage PD (mean disease duration = 2.4 ± 0.4 years), 16 patients with RBD (mean disease duration = 3.8 ± 0.8 years), and 39 age-matched HCs participated in this experiment. All PD patients had their diagnoses confirmed by a licenced neurologist within five years prior to testing to meet our early-stage criterion. Participants had no co-existing diagnosis of dementia or another neurological or psychiatric disease (Hughes et al., 1992). Only PD patients were being treated with dopaminergic therapy. All RBD patients were diagnosed by physicians at the Sleep Disorders Clinic at the London Health Sciences Centre based on v ideo polysomnography and the appropriate diagnostic criteria (American Academy of Sleep Medicine, 2014). Age-matched HCs were within five years of age to their matched patient. Participants with PD and RBD were recruited through the London Health Sciences Centre. Participants abusing alcohol, prescription, or illicit drugs, or taking cognitive-enhancing medications were excluded. Further, we excluded any participants who had a contraindication to MRI.

The Montreal Cognitive Assessment (MoCA) was performed on all

participants to rule out cognitive impairment, with a total MoCA score of 23/30 being used as a cut off (Carson et al., 2018; Nasreddine et al., 2005). The RBD questionnaire Hong Kong (RBDQ-HK) was used to measure clinical RBD symptoms and severity, and to further confirm diagnostic statuses in RBD (Li et al., 2010). RBDQ-HK scores range from 0 to 100, with 18–19 serving as a diagnostic cut-off value for RBD (Li et al., 2010).

The Movement Disorders' Society-Unified Parkinson Disease Rating Scale Part III (MDS-UPDRS-III) was scored by a licenced neurologist with sub-specialty training in movement disorders (P.A.M.) to assess the presence and severity of motor symptoms for all patients off dopaminergic medication (Martinez-Martin et al., 1997). Control and RBD participants were also screened to rule out undiagnosed neurological illness causing motor impairments. Demographic variables, MoCA total, and RBDQ-HK scores are summarized in Table 1. MDS-UPDRS-III scores off dopaminergic therapy, mean disease duration, daily doses of dopamine replacement therapy in terms of levodopa equivalents (LED), and motor deficit dominance (i.e., body side most affected) were also recorded (Table 1). Calculation of daily LED for each patient was based on the theoretical equivalence to levodopa(mg) as follows: levodopa dose(mg) × 1 + levodopa controlled release(mg) × 0.75 + levodopa (mg) × 0.33 if on entacapone(mg) + amantadine(mg) × 0.5 + bromocriptine(mg) × 10 + cabergoline(mg) × 50 + pergolide(mg) × 100 + pramipexole(mg) × 67 + rasagiline(mg) × 100 + ropinirole(mg) × 16.67 + selegiline(mg) × 10 (Wüllner et al., 2010). All participants provided informed written consent to the protocol before beginning the experiment according to the Declaration of Helsinki. This study was approved by the Health Sciences Research Ethics Board of Western University.

2.2. MRI data acquisition

Participants were scanned on a 3 T Siemens MAGNETOM Prisma Fit whole-body scanner at the Centre for Functional and Metabolic Mapping, Western University, London, Ontario, Canada. The scanner had a 32-receiver channel head coil with head position fixation devices installed and a standard body transmit coil was used. A localizer image was obtained first to position participants. T1-weighted (T1w) anatomical scans were obtained for structural information, registration of quantitative maps and diffusion volumes and the segmentation of midbrain nuclei using the CIT168 probabilistic subcortical atlas (Pauli et al., 2018). T1w anatomical images were acquired using a magnetization-prepared rapid gradient echo (MPRAGE) sequence (repetition time (TR) = 2300 ms, echo time (TE) = 2.98 ms, flip angle = 9°, Field of View (FoV) = 256 × 256 mm^2, 159 slices, voxel size = 1 × 1 × 0.9 mm^3, receiver bandwidth = 160 Hz/Px, acquisition time = 5:35 min). High resolution GRE images were acquired with an rf-spoiled, flow compensated 3D gradient echo sequence with six echoes (TE 8.09 ms to 40.49 ms with an interval of 6.48 ms), and (TR = 52 ms, flip angle = 20°, FoV = 224 × 224 mm^2, 96 slices, voxel size = 0.5 × 0.5 × 2 mm^3, receiver bandwidth = 160 Hz/Px, acquisition time = 8:30 min) to generate QSM images (Jenkinson et al., 2012). dMRI scans were acquired for parcellation of striatal subregions through probabilistic tractography. All dMRI scans were acquired using echo-planar imaging sequence (TR = 3800 ms, TE = 88 ms, flip angle = 90°, gradient directions = 95, b1 = 1000 s/mm^2, b2 = 2000 s/mm^2, FoV = 232 × 232 mm^2, 72 slices, voxel size = 2 × 2 × 2 mm^3, receiver bandwidth = 1488 Hz/Px, acquisition time = 7:02 min).

Table 1
Demographic and clinical information for PDs, RBDs, and HCs. Cells show ratio of female to male for sex, age in years, education in years, MoCA total scores, disease duration in years, MDS-UPDRS-III, and RBDQ-HK and body side most affected by PD (i.e., dominant body side L:R). Averages are reported as means ± standard error mean.

	HC	RBD	PD	p-value
Sex (F:M)	21:18	3:13	8:18	**< 0.05**
Age (years)	64.9 ± 1.1	65.4 ± 1.5	66.9 ± 1.4	0.51
Education (years)	15.8 ± 0.5	15.2 ± 0.8	14.2 ± 0.6	0.12
MoCA Total (/30)	28.0 ± 0.3	27.3 ± 0.5	27.5 ± 0.4	0.41
Disease Duration (years)	–	3.8 ± 0.8	2.4 ± 0.4	–
MDS-UPDRS-III (/132)	0.67 ± 0.3	N/A	33.5 ± 3.9	**< 0.001**
RBDQ-HK (/100)	11.5 ± 2.1	42.9 ± 5.0	19.2 ± 5.3	**< 0.001**
Dominant Body Side (L:R)	–	–	11:15	–

2.3. T1-weighted Anatomicals

T1w anatomicals of all participants were skull-stripped using *SynthStrip* (Hoopes et al., 2022) then bias fields for skull-stripped T1w images were corrected using *N4BiasFieldCorrection* from Advanced Normalization Tools (ANTs, version 2.2; https://picsl.upenn.edu/software/ants).

SynthSeg, a deep learning tool was then used to parcellate the whole cortex (Billot et al., 2023). Registration between the MNI152NLin2009cAsym template and subject space was then performed with *greedy* (Yushkevich et al., 2016), for T1w and *SynthSeg* outputs (2 channels), using the normalized cross-correlation cost function with default parameters (Billot et al., 2023). To generate surfaces for the subcortical structures (striatum and VTA/SNc), we generated meshes in the template space and propagated them to each subject. The CIT168 probabilistic atlas (Pauli et al., 2018) segmentation was used to generate a triangulated surface in the template space by creating an isosurface at intensity 0.5, and decimating using 25% (removes 25% of vertices) with PyVista (Sullivan and Kaszynski, 2019). Because of its small size, we customized the approach for the VTA/SNc, by first resampling the images by 200%, creating the isosurface at 0.3, and not performing any decimation.

2.4. Gradient echo magnitude images

Magnitude images from the first echo of the GRE sequence were again skull-stripped using *bet* (Jenkinson et al., 2012). Skull-stripped GRE magnitude images were then linearly registered to the final post-processed T1w images using FMRIB's Linear Image Registration Tool (FLIRT).

2.5. QSM image generation

An in-house singular value decomposition algorithm based on Walsh et al., (2000) was employed to reconstruct the GRE raw data (Klassen and Menon, 2013). This algorithm provides the least squares best estimate of the magnetization and avoids phase singularities. QSM processing was performed as follows: spatial phase unwrapping was accomplished using a 3D best path algorithm (Abdul-Rahman et al., 2007). The frequency at each voxel was then estimated by weighted least squares; each phase echo was weighted by the local signal-to-noise ratio in the corresponding T2*-weighted image. Finally, background removal and dipole inversion were performed simultaneously using a single-step QSM algorithm: https://github.com/AlanKuurstra/qsm_sstv (Chatnuntawech et al., 2017). Since susceptibility values calculated by dipole inversion are relative with unknown offset, an offset was set by forcing the average value within the cerebrospinal fluid to be zero parts per billion (ppb).

Due to low contrast in QSM images, the transformation matrices from the earlier GRE magnitude to T1w image registrations were used to perform linear registration of quantitative maps onto T1w images using FLIRT. QSM images were then offset using the average susceptibility in the cerebrospinal fluid of each participant as an internal reference, which allows for between subject comparisons to be performed (Langkammer et al., 2012).

2.6. Atlas-based segmentation

The CIT168 probabilistic subcortical atlas was used for atlas-based segmentation of the striatum (Pauli et al., 2018). This high-resolution atlas clearly demarcates the regions of interest based on data from young HCs in the Human Connectome Project database. Pre-processed T1w images were registered with the MNI152Nlin2009cAsym template using an initial affine registration using block-matching, followed by deformable b-spline registration, both implemented in NiftyReg v1.3.9 (Modat et al., 2014; Modat et al., 2010). Overlay visualizations depicting the skull-stripping, affine registration, and deformable registration were generated for each subject to check for failures. Failures in affine registration were corrected by forcing initialization with an existing transformation matrix. Discrete and probabilistic segmentation images in the template spaces were automatically propagated to each participant's T1w space, using nearest neighbour interpolation for discrete segmentations, and linear for probabilistic segmentations.

2.7. dMRI pre-processing

All dMRI data was processed using open-source and containerized applications, *snakedwi* and *diffparc*, which use the Brain Imaging Data Structure (BIDS; Gorgolewski et al., 2016) and BIDS apps (Gorgolewski et al., 2017) standards to perform systematized pre-processing, fitting, image registration, and tractography.

dMRI data were pre-processed with denoising using a local principal component analysis method with (dwidenoise from mrtrix3), and correction of ringing artifacts with the *unring* tool (Kellner et al., 2016; Veraart et al., 2016). Eddy current distortions were corrected using *eddy* (FSL), with the –repol option enabled for outlier replacement (Andersson et al., 2016; Andersson and Sotiropoulos, 2016). If multiple phase-encoding directions were collected, *top-up* was used to correct for susceptibility distortions, with the resulting parameters were fed into *eddy* (Andersson et al., 2003). For datasets without multiple phase-encoding directions, we performed a registration-based susceptibility distortion correction with *greedy* (Yushkevich et al., 2016) on the average b0 image

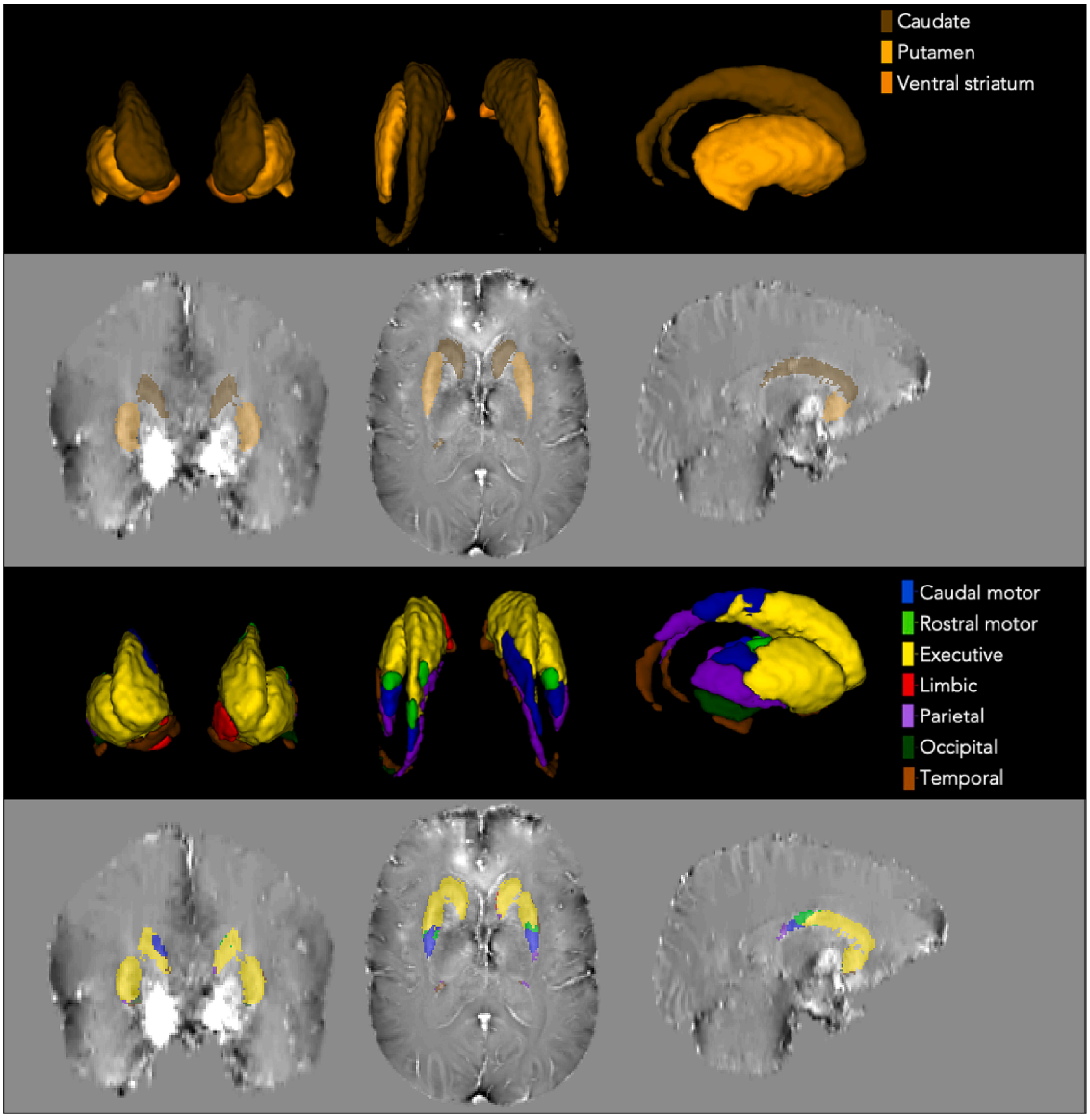

Fig. 1. Striatum parcellation and region of interest segmentation on QSM of a HC. Top two rows show the standard striatum anatomy from the CIT168 atlas in coronal, axial, and sagittal planes. Bottom two rows show the striatum parcellation from probabilistic tractography on the CIT168 atlas in coronal, axial, and sagittal planes with the seven subregions in their respective colours. QSM volumes were registered to T1w images to determine average susceptibility in ppb within each subregional volume averaged between hemispheres.

using the T1w image as a reference. This registration was performed using synthesized T1w-contrast images obtained from the *SynthSR* (Iglesias et al., 2023) tool, to improve registration between the b0 and T1w. Overlay visualizations depicting the skull-stripping and registration were generated to check for failures in each participant. Registration of the final preprocessed diffusion-weighted image to the T1w space was also performed using *SynthSR* to produce images with matched contrast prior to registration. Preprocessed diffusion-weighted image volumes in the T1w space were then used to fit tensors and estimate diffusion tensor metrics using *mrtrix* (Tournier et al., 2012). The fibre orientation distribution (FOD) reconstruction using constrained spherical deconvolution (CSD) was performed by using an FA-based response function, with the number of spherical harmonics (l_max) chosen automatically based on the number of gradient directions.

2.8. Tractography

Tractography was performed from spheres of radius 0.5 mm centered at each vertex, using the iFOD2 algorithm (Tournier et al., 2012). Regions of interest in the MNI152NLin2009cAsym template space were chosen to cover the striatum (i.e., caudate nucleus, putamen, and nucleus accumbens) from the recent CIT168 probabilistic subcortical atlas (Pauli et al., 2018), and cortical labels were built from the Harvard-Oxford atlas, split into seven regions in each hemisphere: limbic, caudal motor, rostral motor, executive, parietal, occipital, and temporal (Fig. 1; Desikan et al., 2006). As we have done previously, in a subject-specific manner, 250 seeds per vertex on the surface of the striatum were initiated to parcellate the striatum into seven subregions, based on the cortical regions to which they were connected (Fig. 1). Volumes of the seven striatal subregions in each hemisphere were then extracted from the parcellation. Masks for each subregion were generated in the T1w space (Fig. 1) to allow for assessment of mean susceptibility averaged across hemispheres in each participants' QSM image registered in their T1w space. All steps in our approach are fully specified or automated, which make them reproducible across centres and better suited for clinical adoption.

2.9. Statistical analysis

Demographic data for participants were compared across groups using one-way ANOVA looking at age, MoCA total scores, and MDS-UPDRS-III scores and a chi-square test was performed for sex. For the regions of interest, PD and RBD patients were compared to HCs, and each other, for the mean susceptibility in parts per billion (ppb) in QSM images. Given that our data was non-normally distributed, per Shapiro-Wilk test, and violated Levene's test for equality of variances, we employed non-parametric tests for our analyses. A Kruskal-Wallis non-parametric test was conducted for each region to assess overall differences across the three groups (early-stage PD, RBD, and HC) and the Dunn's *post hoc* comparisons was conducted to compare individual groups (ie. RBD-HC, PD-HC, and PD-RBD). For all statistical analyses, $p < 0.05$ was used as the statistical threshold. Benjamini-Hochberg correction was used to control the false discovery rate at $q = 0.05$ in our analyses (Benjamini and Hochberg, 1995).

Repeated *k*-folds cross validation and receiver operating characteristic (ROC) curve analysis was performed to assess the potential of our various iron measures to discriminate among the three groups at the single subject level, using MATLAB (version R2021b, MathWorks, Natick, MA, USA). A best cut-off point for sensitivity and specificity was determined using the Youden method. All statistical analyses were performed using IBM SPSS Statistics (version 25, IBM Corp., Armonk, NY, USA). Figures of mean susceptibility were generated using JASP (version 0.17, JASP Team, https://jasp-stats.org/).

3. Results

3.1. Demographics

Our participants did not differ significantly in age, $F(2,78) < 1$, years of education, $F(2,76) = 2.15$, $MSe = 8.9$, $p = 0.12$, $\eta 2_p = 0.05$, or MoCA Total scores, $F(2,78) < 1$. There was a significant difference in sex, $\chi^2(2) = 7.07$, $p = 0.03$, arising from the male dominant patient groups. Early-stage PD patients had an average disease duration of 2.4 ± 0.4 years and RBD patients had an average disease duration of 3.8 ± 0.8 years.

As expected, there were significant differences across groups in the MDS-UPDRS-III score, $F(1,31) = 85.8$, $MSe = 103$, $p < 0.001$, $\eta 2_p = 0.74$, with PD patients showing higher scores. For the PD cohort, the LEDD was 453 ± 55 mg. For the RBDQ–HK, there was a significant difference across groups, $F(2,30) = 18.4$, $MSe = 194$, $p < 0.001$, $\eta 2_p = 0.55$, with RBD patients showing higher values than HCs [$t(26) = 5.95$, $p_{adj} < 0.001$, $d = 2.3$] and PDs [$t(17) = 3.26$, $p_{adj} = 0.01$, $d = 1.70$] and no difference between HC and PD [$t(19) = 1.06$, $p_{adj} = 0.55$, $d = 0.55$] as expected. Higher scores are associated with increased RBD symptom severity and likelihood of presence of RBD pathophysiology. Demographic data for the participants is summarized in Table 1.

3.2. QSM in the standard striatum anatomy

Due to the non-normally distributed data and a significant Levene's test for equality of variances, the Kruskal-Wallis non-parametric test was employed separately in each standard striatum region. There were no significant main effects of Group in the caudate, $H(2) = 2.82$, $p_{adj} = 0.48$, $\eta^2 = 0.01$, putamen, $H(2) = 3.95$, $p_{adj} = 0.34$, $\eta^2 = 0.03$, and nucleus accumbens, $H(2) = 1.75$, $p_{adj} = 0.59$, $\eta^2 = 0.003$, suggesting similar iron deposition across groups (Fig. 2).

$n_{HC} = 39$, $n_{RBD} = 16$, $n_{PD} = 26$.

QSM in the Connectivity-based Parcellated Striatum Anatomy.

Due to the non-normal data and a significant Levene's test for equality of variances, the Kruskal-Wallis non-parametric test was employed separately in each parcellated striatal subregion. In the caudal motor striatum, there was a significant main effect of Group, $H(2) = 10.2$, $p_{adj} = 0.04$, $\eta^2 = 0.11$, suggesting different iron deposition across groups (Fig. 3). Dunn's *post hoc* comparisons revealed significantly lower mean susceptibility in early-stage PD patients, $z = 3.17$, $p_{adj} = 0.005$, suggesting lower iron in PD patients in this subregion (Fig. 3). No significant differences occurred in RBD versus HC, $z = 0.78$, $p_{adj} = 0.99$, or in PD versus RBD, $z = 1.75$, $p_{adj} = 0.24$.

The Kruskal-Wallis non-parametric tests revealed no significant main effects of Group in any other striatal subregion: limbic, $H(2) = 1.35$, $p_{adj} = 0.59$, $\eta^2 = 0.009$, executive, $H(2) = 2.08$, $p_{adj} = 0.59$, $\eta^2 = 0.01$, rostral motor, $H(2) = 1.28$, $p_{adj} = 0.59$, $\eta^2 = 0.008$, parietal, $H(2) = 5.95$, $p_{adj} = 0.26$, $\eta^2 = 0.05$, occipital, $H(2) = 4.63$, $p_{adj} = 0.33$, $\eta^2 = 0.03$, or temporal subregions, $H(2) = 0.70$, $p_{adj} = 0.71$ $\eta^2 = 0.0006$. Mean susceptibility in the caudal motor subregion was the only measure sensitive to group-level changes in early-stage PD patients when compared to HCs (Figs. 3 and 4).

ROC Curve Analyses of the Caudal Motor Striatum and Standard Striatum.

Binary logistic regressions were conducted with the caudal motor striatum mean susceptibility data to perform PD versus HC classification. The predicted probabilities underwent 10 repeated *k*-folds cross validation, and the ROC curve and confusion matrix are shown in Fig. 5 to indicate classification performance. The caudal motor striatum had a mean AUC of 0.80, SEM = 0.02, 95% CI = 0.76 – 0.84, $p < 0.001$, with a sensitivity of 0.88 and specificity of 0.60, and F1 score of 0.67 (Fig. 5).

For comparison, identical ROC curve analyses to the above were conducted with the caudate and putamen mean susceptibility data, which are shown in Fig. 5. The caudate mean susceptibility had a mean AUC of 0.71, SEM = 0.02, with a sensitivity of 0.92, specificity of 0.40, and F1 score of 0.39. The putamen mean susceptibility had a mean AUC

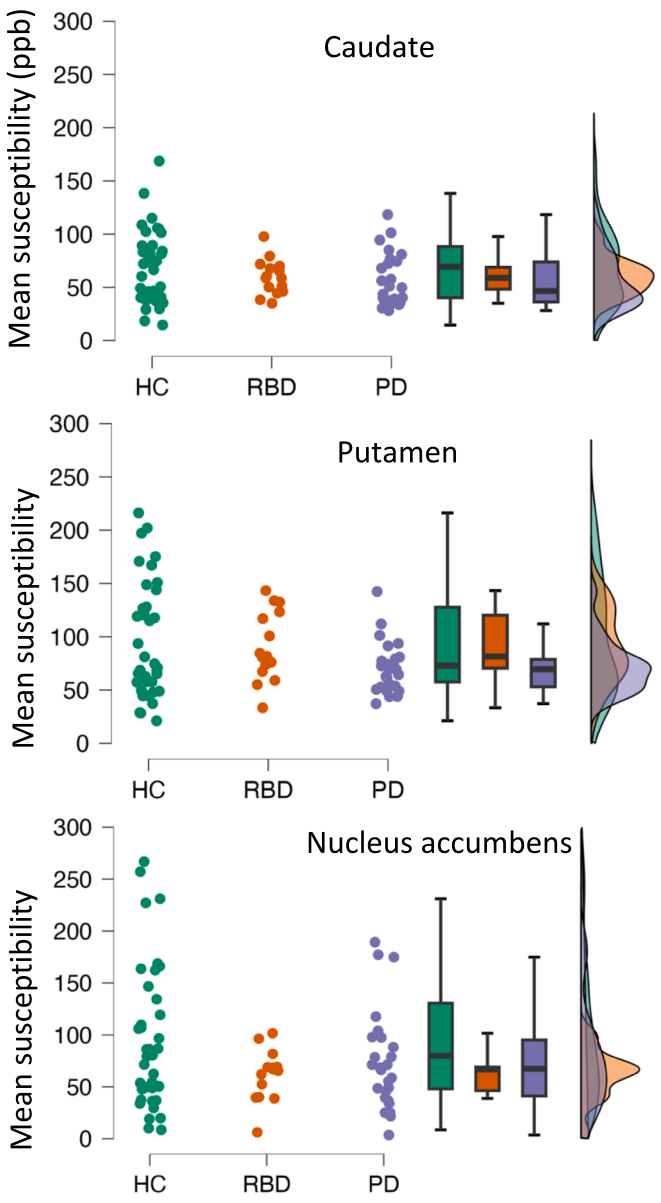

Fig. 2. Mean susceptibility of the Caudate, Putamen, and Nucleus accumbens for HCs, RBD patients and PD patients. Data are shown as scatterplots, boxplots and raincloud plots for the standard striatum region mean susceptibility in ppb. No significant group level differences were found in the caudate, putamen, or nucleus accumbens following correction for multiple comparisons.

of 0.62, SEM = 0.02, with a sensitivity of 0.72, specificity of 0.43, and F1 score of 0.40 (Fig. 5).

4. Conclusions

In this study, we investigated whether pathophysiological changes in the striatum that are known to occur in PD and speculated to arise in RBD, are detected using QSM. Further, we tested whether our tractography-based parcellation technique improves the sensitivity of iron measures from QSM to identify group differences. We only found differences in QSM in the caudal motor subregion of the striatum in early-stage PD patients relative to HCs. That is, early-stage PD patients evidenced significantly lower mean susceptibility in the caudal motor striatum compared to HCs. QSM measures did not differ for PD patients and HCs comparing a) standard parcellations of the striatum (i.e., the caudate nucleus, putamen, and nucleus accumbens) or b) other striatal

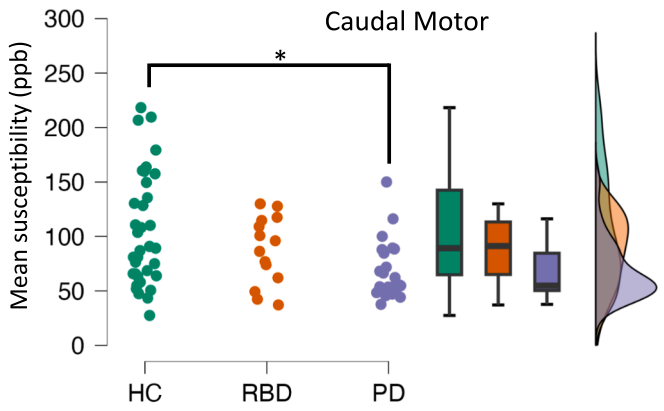

Fig. 3. Mean susceptibility of the Caudal Motor striatal subregion for HCs, RBD patients and PD patients. Data are shown as scatterplots, boxplots and raincloud plots for the caudal motor striatum mean susceptibility in ppb. Significant group level differences were found with PD patients having lower mean susceptibility than HCs and RBD patients showing no differences from HC or PD patients. $n_{HC} = 39$, $n_{RBD} = 16$, $n_{PD} = 26$.

subregions (i.e., rostral motor, executive, temporal, parietal, occipital, and limbic) that are known to be affected later and to a lesser extent in PD patients. Furthermore, a binary logistic regression model using the lone QSM feature that differed between PD patients and HCs at the group level classified PD patients and HCs with good diagnostic accuracy of 0.80. This suggests the potential of caudal motor QSM to contribute to multivariate MRI models for identifying PD patients from HCs at the single-subject level. Application at the single-subject level is required for a diagnostic measure. Though we achieved good diagnostic accuracy, this measure alone would be insufficient for use in clinical practice.

No significant group level differences were found between RBD patients and HCs. Further, no significant group level differences were found between RBD patients and PD patients, which makes interpretation difficult. Larger samples with longer disease durations are needed to determine if RBD patients resemble PD patients or HCs with regards to mean susceptibility in the caudal motor striatum.

4.1. PD

Striatal abnormalities are detected inconsistently with QSM in PD (Ravanfar et al., 2021). Differences in QSM image generation and segmentation (e.g., manual versus atlas-based) could contribute to the variability (Eskreis-Winkler et al., 2017). Further, these inconsistencies could result because standard striatum anatomy demarcation relies on external borders and MRI-visible landmarks, though subregions of the striatum are functionally heterogenous and differentially impacted by PD and its progression (Kish et al., 1988; MacDonald et al., 2013; Ravanfar et al., 2021). Given this, measures of the caudate nucleus, putamen, and nucleus accumbens potentially lack sensitivity to detect pathophysiological changes that affect only small regions of these structures, especially in early PD.

Across this literature, in addition to small sample sizes that can reduce the potential for replication and generalizability of findings, recruitment of patients that differ widely in disease duration within and between studies, will affect the ratio of diseased versus spared striatal substrate. Studies that test a larger proportion of later-staged PD patients will more likely uncover differences in measures of standard striatum structures relative to studies testing earlier-staged PD patients. Combining a review conducted by the Neuroimaging Working Group of the International Parkinson and Movement Disorder Society (MDS; Peralta et al., 2022) with another PD biomarker review (Mitchell et al., 2021) revealed that studies in this literature have a mean disease duration of 4.6 years with a typical PD patient sample of 30 (Mitchell

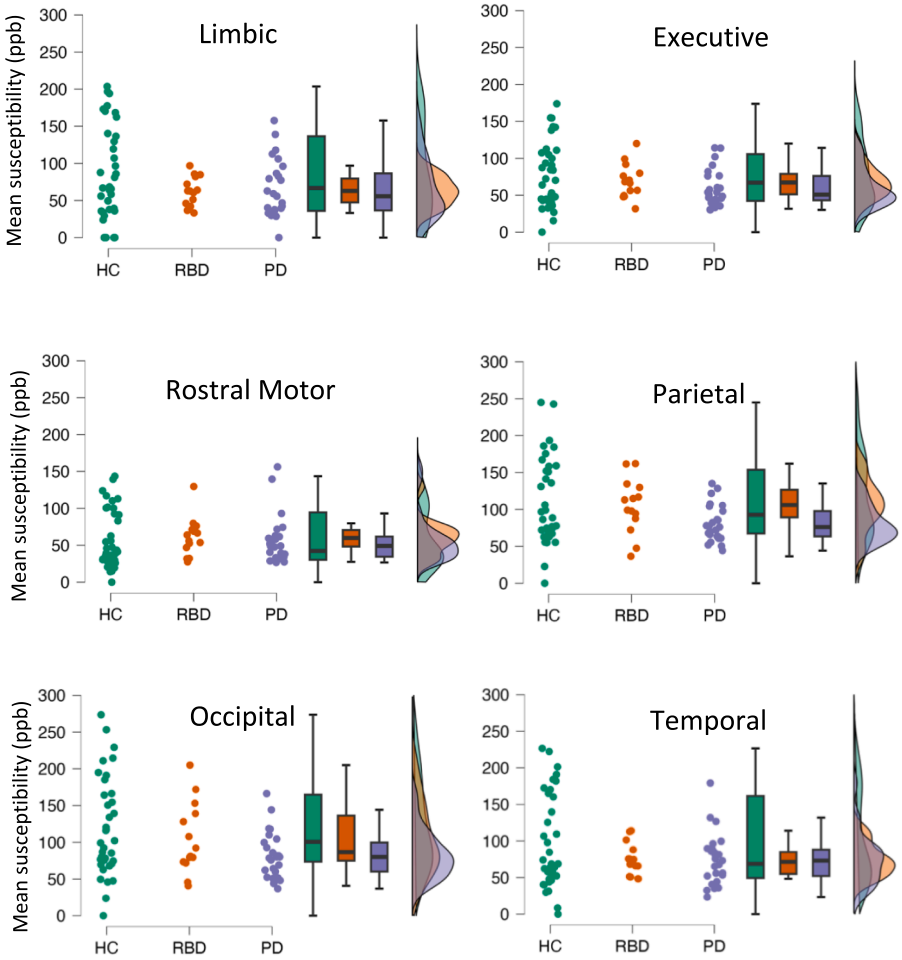

Fig. 4. Mean susceptibility of the Limbic, Executive, Rostral motor, Parietal, Occipital, and Temporal striatal subregion for HCs, RBD patients and PD patients. Data are shown as scatterplots, boxplots and raincloud plots for the mean susceptibility in ppb of the striatal subregions. No significant group level differences were found. $n_{HC} = 39$, $n_{RBD} = 16$, $n_{PD} = 26$.

et al., 2021; Peralta et al., 2022). This mean disease duration cannot be considered early-stage and identifies biomarkers that appear too late in the disease time course for meaningful treatment. Lending credence to these explanations, here we found significant differences between early-staged PD patients (mean disease duration of 2.4 ± 0.4 years) and HCs, using an isolated measure of the caudal motor striatum—the posterior putaminal subregion that is first and most dopamine-depleted in PD based on histology (Fig. 1; Kish et al., 1988). In contrast, in these same data and participants, there were no group differences in QSM measures of the caudate nuclei, putamen, and nucleus accumbens, or the six other striatal subregions that are affected later in PD. These results using QSM replicate our previous findings using volume, in which we found measures in the caudal motor striatum but not the total striatum, caudate nucleus, putamen, or nucleus accumbens different between PD patients and HCs (Khan et al., 2019).

Investigating the potential of our measure to distinguish PD patients at the single-subject level through ROC curve analyses of the caudal motor striatum mean susceptibility, we found a binary logistic regression model that used this single feature had good diagnostic accuracy with an AUC of 0.80 to classify early-stage PD from HC. This falls within the *good* diagnostic accuracy range (i.e., AUC = 0.80 – 0.90), but performs slightly worse than our model which combined dopaminergic midbrain and GP QSM features (i.e., AUC = 0.86; Alushaj et al., submitted). Nine of 43 studies performed ROC curve analyses looking at PD versus HC in QSM in the SN, with AUCs ranging from 0.68 to 0.88 (Ravanfar et al., 2021). It is important to highlight that our single measure of mean susceptibility within the caudal motor *striatum*, a later-affected structure than SN in PD, performs with accuracy that rivals SN related features.

In contrast, the AUC for the caudate nuclei and putamen revealed fair diagnostic accuracy of 0.71 and 0.62 respectively when sorting PD patients from HCs using mean susceptibility (Fig. 5). This suggests our tractography-based parcellation improved the sensitivity and specificity of classifying PD patients from HCs as it achieved a good diagnostic accuracy with AUC of 0.80. This suggests that measures of the *parcellated* striatum might be considered for inclusion in multivariate biomarkers of PD. MRI biomarkers should be prioritized given that they are non-invasive, have moderate cost, and have good clinical availability as compared to other techniques like positron emission tomography or cerebrospinal fluid sampling (Concha-Marambio et al., 2023; Miglis et al., 2021). However, given we are the only group employing this subregional assessment, larger samples are necessary to assess replicability and diagnostic performance of this feature in comparison to other techniques. Inclusion of a *de novo* PD sample may also help to determine when striatal iron changes appear along the disease time course (i.e., at the time of diagnosis or after the early stages of PD).

4.2. RBD

Striatal abnormalities have scarcely been explored using QSM in RBD (Sun et al., 2020). When assessing the prodromal population of RBD patients, no significant group differences were found between RBD

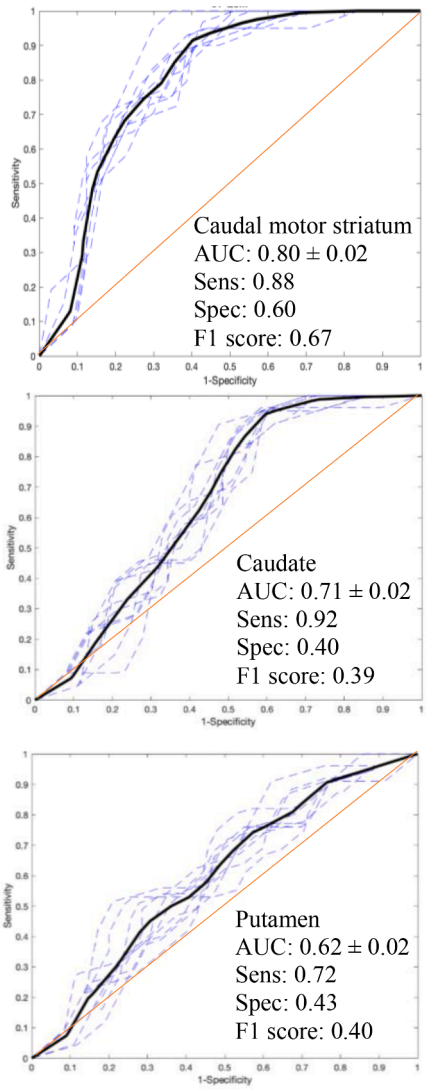

	Predicted	
Observed	HC	PD
HC	23	16
PD	3	23

	Predicted	
Observed	HC	PD
HC	16	23
PD	2	24

	Predicted	
Observed	HC	PD
HC	17	22
PD	7	19

Fig. 5. ROC curve analyses and confusion matrices showing classifications for PD and HC from binomial logistic regression. Data show ROC curves for 10 repeated 5-folds cross validation (dash lines) and the average ROC curve (black line) for 3 T QSM in the caudal motor striatum, caudate, and putamen following binomial logistic regression to classify PD versus HC. AUC, sensitivity, specificity, and F1 score are shown. Diagnostic accuracy is good in when using the caudal motor striatum in PD versus HC and only fair in the caudate and putamen. $n_{HC} = 39$, $n_{PD} = 26$.

patients and HCs in this study, though we applied a tractography-based parcellation to the striatum to focus on the earliest affected subregion in PD. This could be due to a true lack of difference in striatal mean susceptibility at the prodromal stage. Alternatively, QSM and MRI lack sensitivity to detect prodromal changes in the striatum in RBD patients. Further, small sample sizes could be contributing to the lack of group differences. The only other striatal QSM study in RBD also reported no significant differences between 29 RBD patients and 28 HCs with comparable RBDQ-HK scores to our sample (Zhang et al., 2021). In contrast, in our previous work, we identified SNc iron elevation in RBD, which allowed for differentiation of RBD patients from HCs at the single-subject level with good accuracy (Alushaj et al., submitted). This nigral iron elevation could be a precursor to other changes that occur in PD, including lower mean susceptibility in the caudal motor striatum (Alushaj et al., submitted; Sun et al., 2020). Using dMRI measures in the striatum of RBD patients, we detected group level differences from HCs (Alushaj et al., submitted). This finding did not replicate in a sample of RBD patients and HCs from the multicentered Parkinson's Progression Markers Initiative. However, it is important to note that dMRI measures were found to be greatly affected by MRI scanner type, and these large between-scanner differences could have obscured changes in subregional striatal connectivity measures. It is likely that the striatal iron changes occur later than decreased dopamine binding (Frosini et al., 2017; Iranzo et al., 2011) or altered microstructural integrity in RBD patients (Alushaj et al., submitted). As such, measures of the striatum such as iron, dopamine transporter, diffusion of water (measured with dMRI) might have disparate roles across the RBD-PD disease continuum (Iranzo et al., 2011). Comparing QSM and these other techniques directly in the same RBD patients could be revealing.

No differences were found between PD and RBD patients, which could reflect that RBD is specific to alpha-synucleinopathies and not exclusive to PD (Mahowald and Schenck, 2013). We did not find group level differences in mean susceptibility for RBD patients relative to PD patients. This is in line with previous work that failed to reveal significant group-level differences in striatal mean susceptibility. Sun and colleagues (2020) only found marginally lower right putaminal mean susceptibility in PD compared to RBD patients. No significant differences were reported in the caudate or putamen between 25 RBD patients and 50 HCs (Sun et al., 2020). Striatal changes in RBD that resemble those in PD have been reported using other techniques, such as dopamine transporter imaging (Iranzo et al., 2011. It is possible that QSM might lack the sensitivity to detect subtle differences in the striatum that might

distinguish RBD and PD, as well as RBD and HC, though the anticipated larger differences between PD patients and HCs are potentially within the detectable difference range. This could explain our pattern of data. Exploring RBD patients with various disease durations could be revealing and could help to explore this explanation for our findings.

Finally, though iron elevation is a cardinal feature in the SNc, the iron levels of the basal ganglia tell a different story. Previous work suggests a trend toward lower iron levels in PD as compared to HC in the caudate, putamen, and GP (Alushaj et al., submitted; Ravanfar et al., 2021). Histological work revealed lower ferritin levels in the caudate and putamen, but no significant differences in the total iron levels within these structures (Dexter et al., 1991; Griffiths et al., 1999). Iron elevation may not be present in the striatum due to different neuronal populations, lower iron levels, and differential changes across the disease time course (Dexter et al., 1991; Dexter et al., 1989). As such, the QSM narrative may need to shift from iron elevation to altered iron homeostasis in PD within these subcortical structures (Matak et al., 2016). This suggests "optimal" iron level ranges may exist such that deviations that are either too high or too low may contribute to disease processes.

5. Limitations

Our RBD sample was smaller than the other two groups but is of comparable size to previous QSM literature and is still an *isolated* RBD cohort without Parkinsonian motor symptoms (Lee et al., 2014; Sun et al., 2020; Zhang et al., 2021). Our RBD cohort was male-dominant which necessitates further work to balance samples to generate sex-specific models to better account for sex differences across groups. To increase replicability, we used a single atlas for segmentation, which was developed in a younger cohort (mean age of 35) than our participants (Pauli et al., 2018). Given that we used the same atlas on all participants, any ageing differences would equally impact our age-matched samples (Persson et al., 2015).

Probabilistic tractography has its own limitations regarding false positive and negatives based on connections in regions with complex fiber orientations, which can impact the volumes generated in our downstream analyses (Jeurissen et al., 2019; Tournier et al., 2012). Furthermore, we employed just one model to estimate tissue diffusion, thus a different model could lead to different results as could a different probability of connection threshold (Daducci et al., 2012). Lastly, the assigned volumes are based on probability of connection and does not reflect strength of connection or directionality (Jones, 2010; Thomas et al., 2014).

There is no gold standard approach to QSM; various algorithms are used to best handle the estimation of local tissue magnetic susceptibility (Chatnuntawech et al., 2017; Langkammer et al., 2018; Rasmussen et al., 2018). Our approach is one of many techniques which could be used to detect group differences (Biondetti et al., 2021). Previous work has also reported significant correlations between susceptibility values of standard striatum and cognitive dysfunction measured by the MoCA (Uchida et al., 2020; Uchida et al., 2019). Furthermore, additional quantitative techniques are available beyond QSM; R2* relaxometry was not assessed in this study given its lower sensitivity to PD iron elevation (Alushaj, 2019; Langkammer et al., 2016).

QSM is not purely associated with iron, as calcium and myelin can have diamagnetic influences on susceptibility (Buch et al., 2015; Hametner et al., 2018; Lee et al., 2021). Furthermore, larger regions of interest may be prone to signal averaging, loss of contrast information, and have greater microstructural tissue differences within them, which are not easily captured using our approach (Hametner et al., 2018). Lastly, the striatum is not as iron-rich as the substantia nigra or globus pallidus which can complicate interpretation (Hallgren and Sourander, 1958).

There is a need to establish bigger cohorts to develop separate train and test sets for analyses of group differences and accuracies in biomarker classification tests. Establishing openly available QSM datasets would allow for stratifying patients on various measures such as disease duration.

5.1. Summary

Our findings suggest that pathophysiological changes in the striatum can be effectively detected using QSM and MRI in PD relative to HCs but, not relative to RBD. QSM did not differ in RBD patients relative to HCs, even at the group level. We also demonstrated that parcellation of the striatum, enabling targeted measures of the earliest and most affected region in PD–the caudal motor subregion—increases the sensitivity of QSM and MRI to detect group-level differences. In fact, group-level differences in QSM between PD patients and HCs only occurred in this subregion of the striatum. QSM in caudal motor striatum detect PD even at the single-subject level with good accuracy. Our approach uses publicly available atlases to define the striatum and cortex. Our methods can be reproduced by individuals with no specialized neuroradiological training. Given these features and our findings, isolating the most PD-sensitive subregion—the caudal motor striatum—using our parcellation technique and extracting QSM could contribute to multivariate or multimodal diagnostic measures of PD. QSM in caudal motor striatum alone, however, does not appear to have the sensitivity and specificity to act as a biomarker in a clinical setting. Biomarkers of PD would simplify the diagnosis and would improve the power of clinical trials to detect disease-modifying therapies. Ideally, identifying neural changes present in RBD that predict PD could provide preclinical biomarkers, as well as of measures of progression to PD, which might allow introducing potential disease modifying therapies at earlier stages in the disease progression when they are expected to have the greatest effects.

CRediT authorship contribution statement

Erind Alushaj: Conceptualization, Methodology, Investigation, Formal analysis, Writing – original draft, Visualization. **Dimuthu Hemachandra:** Writing – review & editing. **Alan Kuurstra:** Software, Writing – review & editing. **Ravi S. Menon:** Software, Writing – review & editing. **Hooman Ganjavi:** Resources, Writing – review & editing. **Manas Sharma:** Writing – review & editing. **Alia Kashgari:** Resources, Writing – review & editing. **Jennifer Barr:** Resources, Writing – review & editing. **William Reisman:** Resources, Writing – review & editing. **Ali R. Khan:** Software, Methodology, Resources, Writing – review & editing, Supervision. **Penny A. MacDonald:** Writing – review & editing, Funding acquisition, Supervision.

Declaration of Competing Interest

The authors declare that they have no known competing financial interests or personal relationships that could have appeared to influence the work reported in this paper.

Data availability

The data that support the findings of this study are available from the corresponding author following a formal data sharing agreement, approval from the requester's local ethics committee, and submission of a formal project outline. Code for R2* relaxometry and QSM image generation is available at (https://github.com/AlanKuurstra/qsm_sstv).

Acknowledgements

This work was supported by a BrainsCAN Accelerator Grant ("Investigating VTA, SNc and dopamine projections in the brain using MRI") arising from the Canada First Research Excellence Fund awarded to Dr. Penny MacDonald, Dr. Ali Khan, and Dr. Ravi Menon, and a Canadian Institute of Health Research Project Grant ("Advancing Clinically-Useful Diagnostic and Progression Markers of PD with

Neuroimaging", 201903) awarded to Dr. Penny MacDonald and Dr. Ali Khan.

References

Abdul-Rahman, H.S., Gdeisat, M.A., Burton, D.R., Lalor, M.J., Lilley, F., Moore, C.J., 2007. Fast and robust three-dimensional best path phase unwrapping algorithm. Applied Optics 46, 6623–6635. https://doi.org/10.1364/AO.46.006623.

Alushaj, E., 2019. Differentiating the substantia nigra and ventral tegmental area in early-stage parkinson's disease using iron imaging (Monograph). Western University.

American Academy of Sleep Medicine, 2014. International classification of sleep disorders - (ICSD-3), Third. ed. American Academy of Sleep Medicine, Darien, IL.

Andersson, J.L.R., Skare, S., Ashburner, J., 2003. How to correct susceptibility distortions in spin-echo echo-planar images: Application to diffusion tensor imaging. NeuroImage 20, 870–888. https://doi.org/10.1016/S1053-8119(03)00336-7.

Andersson, J.L.R., Sotiropoulos, S.N., 2016. An integrated approach to correction for off-resonance effects and subject movement in diffusion MR imaging. NeuroImage 125, 1063–1078. https://doi.org/10.1016/j.neuroimage.2015.10.019.

Andersson, J.L.R., Graham, M.S., Zsoldos, E., Sotiropoulos, S.N., 2016. Incorporating outlier detection and replacement into a non-parametric framework for movement and distortion correction of diffusion MR images. NeuroImage 141, 556–572. https://doi.org/10.1016/j.neuroimage.2016.06.058.

Barber, T.R., Klein, J.C., Mackay, C.E., Hu, M.T.M., 2017. Neuroimaging in pre-motor parkinson's disease. Neuroimage Clin 15, 215–227. https://doi.org/10.1016/j.nicl.2017.04.011.

Barone, P., Antonini, A., Colosimo, C., Marconi, R., Morgante, L., Avarello, T.P., Bottacchi, E., Cannas, A., Ceravolo, G., Ceravolo, R., Cicarelli, G., Gaglio, R.M., Giglia, R.M., Iemolo, F., Manfredi, M., Meco, G., Nicoletti, A., Pederzoli, M., Petrone, A., Pisani, A., Pontieri, F.E., Quatrale, R., Ramat, S., Scala, R., Volpe, G., Zappulla, S., Bentivoglio, A.R., Stocchi, F., Trianni, G., Dotto, P.D., group, P. study, 2009. The PRIAMO study: A multicenter assessment of nonmotor symptoms and their impact on quality of life in Parkinson's disease. Mov Disord 24, 1641–1649. https://doi.org/10.1002/mds.22643.

Benjamini, Y., Hochberg, Y., 1995. Controlling the false discovery rate: A practical and powerful approach to multiple testing. Journal of the Royal Statistical Society: Series B (Methodological) 57, 289–300. https://doi.org/10.1111/j.2517-6161.1995.tb02031.x.

Billot, B., Greve, D.N., Puonti, O., Thielscher, A., Van Leemput, K., Fischl, B., Dalca, A.V., Iglesias, J.E., 2023. SynthSeg: Segmentation of brain MRI scans of any contrast and resolution without retraining. Medical Image Analysis 86, 102789.

Biondetti, E., Santin, M.D., Valabrègue, R., Mangone, G., Gaurav, R., Pyatigorskaya, N., Hutchison, M., Yahia-Cherif, L., Villain, N., Habert, M.O., Arnulf, I., Leu-Semenescu, S., Dodet, P., Vila, M., Corvol, J.C., Vidailhet, M., Lehéricy, S., 2021. The spatiotemporal changes in dopamine, neuromelanin and iron characterizing parkinson's disease. Brain 144, 3114–3125. https://doi.org/10.1093/brain/awab191.

Buch, S., Liu, S., Ye, Y., Cheng, Y.-C.-N., Neelavalli, J., Haacke, E.M., 2015. Susceptibility mapping of air, bone, and calcium in the head. Magnetic Resonance in Medicine 73, 2185–2194. https://doi.org/10.1002/mrm.25350.

Cao, J.Y., Dixon, S.J., 2016. Mechanisms of ferroptosis. Cellular and Molecular Life Sciences 73, 2195–2209. https://doi.org/10.1007/s00018-016-2194-1.

Carson, N., Leach, L., Murphy, K.J., 2018. A re-examination of montreal cognitive assessment (MoCA) cutoff scores. International Journal of Geriatric Psychiatry 33, 379–388. https://doi.org/10.1002/gps.4756.

Chatnuntawech, I., McDaniel, P., Cauley, S.F., Gagoski, B.A., Langkammer, C., Martin, A., Grant, P.E., Wald, L.L., Setsompop, K., Adalsteinsson, E., Bilgic, B., 2017. Single-step quantitative susceptibility mapping with variational penalties. NMR in Biomedicine 30. https://doi.org/10.1002/nbm.3570.

Cheng, H.C., Ulane, C.M., Burke, R.E., 2010. Clinical progression in parkinson disease and the neurobiology of axons. Annals of Neurology 67, 715–725. https://doi.org/10.1002/ana.21995.

Concha-Marambio, L., Weber, S., Farris, C.M., Dakna, M., Lang, E., Wicke, T., Ma, Y., Starke, M., Ebentheuer, J., Sixel-Döring, F., Muntean, M.L., Schade, S., Trenkwalder, C., Soto, C., Mollenhauer, B., 2023. Accurate detection of α-Synuclein seeds in cerebrospinal fluid from isolated rapid eye movement sleep behavior disorder and patients with parkinson's disease in the DeNovo Parkinson (DeNoPa) cohort. movement disorders. https://doi.org/10.1002/mds.29329.

Daducci, A., Gerhard, S., Griffa, A., Lemkaddem, A., Cammoun, L., Gigandet, X., Meuli, R., Hagmann, P., Thiran, J.-P., Hess, C.P., 2012. The connectome mapper: An Open-Source processing pipeline to Map connectomes with MRI. PLoS One1 7 (12), e48121.

Desikan, R.S., Ségonne, F., Fischl, B., Quinn, B.T., Dickerson, B.C., Blacker, D., Buckner, R.L., Dale, A.M., Maguire, R.P., Hyman, B.T., Albert, M.S., Killiany, R.J., 2006. An automated labeling system for subdividing the human cerebral cortex on MRI scans into gyral based regions of interest. NeuroImage 31, 968–980. https://doi.org/10.1016/j.neuroimage.2006.01.021.

Dexter, D.T., Wells, F.R., Lee, A.J., Agid, F., Agid, Y., Jenner, P., Marsden, C.D., 1989. increased nigral iron content and alterations in other metal Ions occurring in brain in parkinson's disease. Journal of Neurochemistry 52, 1830–1836. https://doi.org/10.1111/j.1471-4159.1989.tb07264.x.

Dexter, D.T., Carayon, A., Javoy-agid, F., Agid, Y., Wells, F.R., Daniel, S.E., Lees, A.J., Jenner, P., Marsden, C.D., 1991. Alterations in the levels of iron, ferritin and other trace metals in parkinson's disease and other neurodegenerative diseases affecting the basal ganglia. Brain 114 (4), 1953–1975.

Dixon, S.J., Lemberg, K.M., Lamprecht, M.R., Skouta, R., Zaitsev, E.M., Gleason, C.E., Patel, D.N., Bauer, A.J., Cantley, A.M., Yang, W.S., Morrison 3rd, B., Stockwell, B.R., 2012. Ferroptosis: an iron-dependent form of nonapoptotic cell death. Cell 149, 1060–1072. https://doi.org/10.1016/j.cell.2012.03.042.

Dorsey, E.R., Sherer, T., Okun, M.S., Bloem, B.R., Brundin, P., Langston, J.W., Bloem, B. R., 2018. the emerging evidence of the parkinson pandemic. Journal of Parkinson's Disease 8 (s1), S3–S8.

Du, G., Liu, T., Lewis, M.M., Kong, L., Wang, Y., Connor, J., Mailman, R.B., Huang, X., 2016. Quantitative susceptibility mapping of the midbrain in parkinson's disease. Movement Disorders 31, 317–324. https://doi.org/10.1002/mds.26417.

Emre, M., Ford, P.J., Bilgiç, B., Uç, E.Y., 2014. Cognitive impairment and dementia in parkinson's disease: Practical issues and management. Movement Disorders 29, 663–672. https://doi.org/10.1002/mds.25870.

Eskreis-Winkler, S., Zhang, Y., Zhang, J., Liu, Z., Dimov, A., Gupta, A., Wang, Y., 2017. The clinical utility of QSM: disease diagnosis, medical management, and surgical planning. NMR in Biomedicine 30. https://doi.org/10.1002/nbm.3668.

Frosini, D., Cosottini, M., Donatelli, G., Costagli, M., Biagi, L., Pacchetti, C., Terzaghi, M., Cortelli, P., Arnaldi, D., Bonanni, E., Tosetti, M., Bonuccelli, U., Ceravolo, R., 2017. Seven tesla MRI of the substantia nigra in patients with rapid eye movement sleep behavior disorder. Parkinsonism & Related Disorders 43, 105–109. https://doi.org/10.1016/j.parkreldis.2017.08.002.

Gorgolewski, K.J., Auer, T., Calhoun, V.D., Craddock, R.C., Das, S., Duff, E.P., Flandin, G., Ghosh, S.S., Glatard, T., Halchenko, Y.O., Handwerker, D.A., Hanke, M., Keator, D., Li, X., Michael, Z., Maumet, C., Nichols, B.N., Nichols, T.E., Pellman, J., Poline, J.B., Rokem, A., Schaefer, G., Sochat, V., Triplett, W., Turner, J.A., Varoquaux, G., Poldrack, R.A., 2016. The brain imaging data structure, a format for organizing and describing outputs of neuroimaging experiments. Scientific Data 3. https://doi.org/10.1038/sdata.2016.44.

Gorgolewski, K.J., Alfaro-Almagro, F., Auer, T., Bellec, P., Capotă, M., Chakravarty, M. M., Churchill, N.W., Cohen, A.L., Craddock, R.C., Devenyi, G.A., Eklund, A., Esteban, O., Flandin, G., Ghosh, S.S., Guntupalli, J.S., Jenkinson, M., Keshavan, A., Kiar, G., Liem, F., Raamana, P.R., Raffelt, D., Steele, C.J., Quirion, P.-O., Smith, R.E., Strother, S.C., Varoquaux, G., Wang, Y., Yarkoni, T., Poldrack, R.A., Schneidman, D., 2017. BIDS apps: Improving ease of use, accessibility, and reproducibility of neuroimaging data analysis methods. PLoS Computational Biology 13 (3), e1005209.

Griffiths, P.D., Dobson, B.R., Jones, G.R., Clarke, D.T., 1999. Iron in the basal ganglia in parkinson's disease An in vitro study using extended x-ray absorption fine structure and cryo-electron microscopy. Brain 122, 667–673.

Hallgren, B., Sourander, P., 1958. the effect of age on the non-haemin iron in the human brain. Journal of Neurochemistry 3 (1), 41–51.

Hametner, S., Endmayr, V., Deistung, A., Palmrich, P., Prihoda, M., Haimburger, E., Menard, C., Feng, X., Haider, T., Leisser, M., Kock, U., Kaider, A., Hoftberger, R., Robinson, S., Reichenbach, J.R., Lassmann, H., Traxler, H., Trattnig, S., Grabner, G., 2018. The influence of brain iron and myelin on magnetic susceptibility and effective transverse relaxation - A biochemical and histological validation study. NeuroImage 179, 117–133. https://doi.org/10.1016/j.neuroimage.2018.06.007.

Hare, D.J., Double, K.L., 2016. Iron and dopamine: a toxic couple. Brain 139, 1026–1035. https://doi.org/10.1093/brain/aww022.

Hogl, B., Stefani, A., Videnovic, A., 2018. Idiopathic REM sleep behaviour disorder and neurodegeneration - an update. Nature Reviews. Neurology 14, 40–55. https://doi.org/10.1038/nrneurol.2017.157.

Hoopes, A., Mora, J.S., Dalca, A.V., Fischl, B., Hoffmann, M., 2022. SynthStrip: skull-stripping for any brain image. NeuroImage 260, 119474.

Hughes, A.J., Daniel, S.E., Kilford, L., Lees, A.J., 1992. Accuracy of clinical diagnosis of idiopathic parkinson's disease: a clinico-pathological study of 100 cases. Journal of Neurology, Neurosurgery, and Psychiatry 55, 181–184. https://doi.org/10.1136/jnnp.55.3.181.

Iglesias, J.E., Billot, B., Balbastre, Y., Magdamo, C., Arnold, S.E., Das, S., Edlow, B.L., Alexander, D.C., Golland, P., Fischl, B., 2023. SynthSR: A public AI tool to turn heterogeneous clinical brain scans into high-resolution T1-weighted images for 3D morphometry. Science Advances 9 (5).

Iranzo, A., Valldeoriola, F., Lomeña, F., Molinuevo, J.L., Serradell, M., Salamero, M., Cot, A., Ros, D., Pavía, J., Santamaria, J., Tolosa, E., 2011. Serial dopamine transporter imaging of nigrostriatal function in patients with idiopathic rapid-eye-movement sleep behaviour disorder: a prospective study. Lancet Neurology 10, 797–805. https://doi.org/10.1016/s1474-4422(11)70152-1.

Iranzo, A., Fernández-Arcos, A., Tolosa, E., Serradell, M., Molinuevo, J.L., Valldeoriola, F., Gelpi, E., Vilaseca, I., Sánchez-Valle, R., Lladó, A., Gaig, C., Santamaría, J., Toft, M., 2014. Neurodegenerative disorder risk in idiopathic REM sleep behavior disorder: study in 174 patients. PLoS One1 9 (2), e89741.

Jenkinson, M., Beckmann, C.F., Behrens, T.E.J., Woolrich, M.W., Smith, S.M., 2012. FSL. FSL. Neuroimage 62 (2), 782–790.

Jeurissen, B., Descoteaux, M., Mori, S., Leemans, A., 2019. Diffusion MRI fiber tractography of the brain. NMR in Biomedicine 32 (4). https://doi.org/10.1002/nbm.3785.

Jones, D.K., 2010. Challenges and limitations of quantifying brain connectivity in vivo with diffusion MRI. Imaging Med 2 (3), 341–355.

Kellner, E., Dhital, B., Kiselev, V.G., Reisert, M., 2016. Gibbs-ringing artifact removal based on local subvoxel-shifts. Magnetic Resonance in Medicine 76, 1574–1581. https://doi.org/10.1002/mrm.26054.

Khan, A.R., Hiebert, N.M., Vo, A., Wang, B.T., Owen, A.M., Seergobin, K.N., MacDonald, P.A., 2019. Biomarkers of parkinson's disease: Striatal sub-regional structural morphometry and diffusion MRI. Neuroimage Clin 21, 101597. https://doi.org/10.1016/j.nicl.2018.11.007.

Kish, S.J., Shannak, K., Hornykiewicz, O., 1988. Uneven pattern of dopamine loss in the striatum of patients with idiopathic parkinson's disease. Pathophysiologic and clinical implications. The New England Journal of Medicine 318, 876–880. https://doi.org/10.1056/NEJM198804073181402.

Klassen, L.M., Menon, R.S., 2013. Optimal Phase Sensitive Combination of Multi-channel, Multi-echo Images, in. Salt Lake City, Utah.

Langkammer, C., Schweser, F., Krebs, N., Deistung, A., Goessler, W., Scheurer, E., Sommer, K., Reishofer, G., Yen, K., Fazekas, F., Ropele, S., Reichenbach, J.R., 2012. Quantitative susceptibility mapping (QSM) as a means to measure brain iron? A post mortem validation study. NeuroImage 62, 1593–1599. https://doi.org/10.1016/j.neuroimage.2012.05.049.

Langkammer, C., Pirpamer, L., Seiler, S., Deistung, A., Schweser, F., Franthal, S., Homayoon, N., Katschnig-Winter, P., Koegl-Wallner, M., Pendl, T., Stoegerer, E.M., Wenzel, K., Fazekas, F., Ropele, S., Reichenbach, J.R., Schmidt, R., Schwingenschuh, P., Kassubek, J., 2016. Quantitative susceptibility mapping in parkinson's disease. PLoS One1 11 (9), e0162460.

Langkammer, C., Schweser, F., Shmueli, K., Kames, C., Li, X., Guo, L., Milovic, C., Kim, J., Wei, H., Bredies, K., Buch, S., Guo, Y., Liu, Z., Meineke, J., Rauscher, A., Marques, J. P., Bilgic, B., 2018. Quantitative susceptibility mapping: Report from the 2016 reconstruction challenge. Magnetic Resonance in Medicine 79, 1661–1673. https://doi.org/10.1002/mrm.26830.

Lee, H., Cho, H., Lee, M.J., Kim, T.-H., Roh, J., Lee, J.-H., 2021. Differential effect of iron and myelin on susceptibility MRI in the substantia nigra. Radiology 301, 682–691. https://doi.org/10.1148/radiol.2021210116.

Lee, J.H., Han, Y.H., Cho, J.W., Lee, J.S., Lee, S.J., Kim, D.J., Kim, T.H., Kang, B.M., Kim, T.H., Mun, C.W., 2014. Evaluation of brain iron content in idiopathic REM sleep behavior disorder using quantitative magnetic resonance imaging. Parkinsonism & Related Disorders 20, 776–778. https://doi.org/10.1016/j.parkreldis.2014.03.023.

Lehericy, S., Vaillancourt, D.E., Seppi, K., Monchi, O., Rektorova, I., Antonini, A., McKeown, M.J., Masellis, M., Berg, D., Rowe, J.B., Lewis, S.J.G., Williams-Gray, C. H., Tessitore, A., Siebner, H.R., 2017. the role of high-field magnetic resonance imaging in parkinsonian disorders: Pushing the boundaries forward. Movement Disorders 32 (4), 510–525.

Li, S.X., Wing, Y.K., Lam, S.P., Zhang, J., Yu, M.W., Ho, C.K., Tsoh, J., Mok, V., 2010. Validation of a new REM sleep behavior disorder questionnaire (RBDQ-HK). Sleep Medicine 11, 43–48. https://doi.org/10.1016/j.sleep.2009.06.008.

MacDonald, A.A., Monchi, O., Seergobin, K.N., Ganjavi, H., Tamjeedi, R., MacDonald, P. A., 2013. Parkinson's disease duration determines effect of dopaminergic therapy on ventral striatum function. Movement Disorders 28, 153–160. https://doi.org/10.1002/mds.25152.

Mahowald, M.W., Schenck, C.H., 2013. REM sleep behaviour disorder: a marker of synucleinopathy. Lancet Neurology 12, 417–419. https://doi.org/10.1016/S1474-4422(13)70078-4.

Martinez-Martin, P., Garcia Urra, D., del Ser Quijano, T., Balseiro Gomez, J., Gomez Utrero, E., Pineiro, R., Andres, M.T., 1997. A new clinical tool for gait evaluation in parkinson's disease. Clinical Neuropharmacology 20, 183–194.

Matak, P., Matak, A., Moustafa, S., Aryal, D.K., Benner, E.J., Wetsel, W., Andrews, N.C., 2016. Disrupted iron homeostasis causes dopaminergic neurodegeneration in mice. Proceedings of the National Academy of Sciences of the United States of America 113, 3428–3435. https://doi.org/10.1073/pnas.1519473113.

Miglis, M.G., Adler, C.H., Antelmi, E., Arnaldi, D., Baldelli, L., Boeve, B.F., Cesari, M., Dall'Antonia, I., Diederich, N.J., Doppler, K., Dušek, P., Ferri, R., Gagnon, J.-F., Gan-Or, Z., Hermann, W., Högl, B., Hu, M.T., Iranzo, A., Janzen, A., Kuzkina, A., Lee, J.-Y., Leenders, K.L., Lewis, S.J.G., Liguori, C., Liu, J., Lo, C., Ehgoetz Martens, K.A., Nepozitek, J., Plazzi, G., Provini, F., Puligheddu, M., Rolinski, M., Rusz, J., Stefani, A., Summers, R.L.S., Yoo, D., Zitser, J., Oertel, W.H., 2021. Biomarkers of conversion to α-synucleinopathy in isolated rapid-eye-movement sleep behaviour disorder. Lancet Neurology 20 (8), 671–684.

Mitchell, T., Lehéricy, S., Chiu, S.Y., Strafella, A.P., Stoessl, A.J., Vaillancourt, D.E., 2021. Emerging neuroimaging biomarkers across disease stage in parkinson disease: A review. JAMA Neurology 78 (10), 1262.

Modat, M., Ridgway, G.R., Taylor, Z.A., Lehmann, M., Barnes, J., Hawkes, D.J., Fox, N.C., Ourselin, S., 2010. Fast free-form deformation using graphics processing units. Computer Methods and Programs in Biomedicine 98, 278–284. https://doi.org/10.1016/j.cmpb.2009.09.002.

Modat, M., Cash, D.M., Daga, P., Winston, G.P., Duncan, J.S., Ourselin, S., 2014. Global image registration using a symmetric block-matching approach. J Med Imaging (Bellingham) 1, 24003. https://doi.org/10.1117/1.JMI.1.2.024003.

Nasreddine, Z.S., Phillips, N.A., Bedirian, V., Charbonneau, S., Whitehead, V., Collin, I., Cummings, J.L., Chertkow, H., 2005. The montreal cognitive assessment, MoCA: a brief screening tool for mild cognitive impairment. Journal of the American Geriatrics Society 53, 695–699. https://doi.org/10.1111/j.1532-5415.2005.53221.x.

Pauli, W.M., Nili, A.N., Tyszka, J.M., 2018. A high-resolution probabilistic in vivo atlas of human subcortical brain nuclei. Scientific Data 5, 180063. https://doi.org/10.1038/sdata.2018.63.

Peralta, C., Strafella, A.P., van Eimeren, T., Ceravolo, R., Seppi, K., Kaasinen, V., Arena, J.E., Lehericy, S., 2022. Pragmatic approach on neuroimaging techniques for the differential diagnosis of parkinsonisms. Mov Disord Clin Pract 9 (1), 6–19.

Peran, P., Cherubini, A., Assogna, F., Piras, F., Quattrocchi, C., Peppe, A., Celsis, P., Rascol, O., Demonet, J.F., Stefani, A., Pierantozzi, M., Pontieri, F.E., Caltagirone, C., Spalletta, G., Sabatini, U., 2010. Magnetic resonance imaging markers of parkinson's disease nigrostriatal signature. Brain 133, 3423–3433. https://doi.org/10.1093/brain/awq212.

Persson, N., Wu, J., Zhang, Q., Liu, T.T., Shen, J., Bao, R., Ni, M., Liu, T.T., Wang, Y., Spincemaille, P., 2015. Age and sex related differences in subcortical brain iron concentrations among healthy adults. NeuroImage 122, 385–398. https://doi.org/10.1016/j.neuroimage.2015.07.050.

Postuma, R.B., Aarsland, D., Barone, P., Burn, D.J., Hawkes, C.H., Oertel, W., Ziemssen, T., 2012. Identifying prodromal parkinson's disease: pre-motor disorders in parkinson's disease. Movement Disorders 27, 617–626. https://doi.org/10.1002/mds.24996.

Postuma, R.B., Berg, D., 2016. Advances in markers of prodromal parkinson disease. Nature Reviews. Neurology 12, 622–634. https://doi.org/10.1038/nrneurol.2016.152.

Postuma, R.B., Iranzo, A., Hu, M., Högl, B., Boeve, B.F., Manni, R., Oertel, W.H., Arnulf, I., Ferini-Strambi, L., Puligheddu, M., Antelmi, E., Cochen De Cock, V., Arnaldi, D., Mollenhauer, B., Videnovic, A., Sonka, K., Jung, K.-Y., Kunz, D., Dauvilliers, Y., Provini, F., Lewis, S.J., Buskova, J., Pavlova, M., Heidbreder, A., Montplaisir, J.Y., Santamaria, J., Barber, T.R., Stefani, A., St.Louis, E.K., Terzaghi, M., Janzen, A., Leu-Semenescu, S., Plazzi, G., Nobili, F., Sixel-Doering, F., Dusek, P., Bes, F., Cortelli, P., Ehgoetz Martens, K., Gagnon, J.-F., Gaig, C., Zucconi, M., Trenkwalder, C., Gan-Or, Z., Lo, C., Rolinski, M., Mahlknecht, P., Holzknecht, E., Boeve, A.R., Teigen, L.N., Toscano, G., Mayer, G., Morbelli, S., Dawson, B., Pelletier, A., 2019. Risk and predictors of dementia and parkinsonism in idiopathic REM sleep behaviour disorder: a multicentre study. Brain 142 (3), 744–759.

Prasad, S., Saini, J., Yadav, R., Pal, P.K., 2018. Motor asymmetry and neuromelanin imaging: Concordance in parkinson's disease. Parkinsonism & Related Disorders 53, 28–32. https://doi.org/10.1016/j.parkreldis.2018.04.022.

Pyatigorskaya, N., Sanz-Morère, C.B., Gaurav, R., Biondetti, E., Valabregue, R., Santin, M., Yahia-Cherif, L., Lehéricy, S., 2020. Iron imaging as a diagnostic tool for parkinson's disease: A systematic review and Meta-Analysis. Frontiers in Neurology 11. https://doi.org/10.3389/fneur.2020.00366.

Rasmussen, K.G.B., Kristensen, M.J., Blendal, R.G., Ostergaard, L.R., Plocharski, M., O'Brien, K., Langkammer, C., Janke, A., Barth, M., Bollmann, S., 2018. DeepQSM - Using deep learning to solve the dipole inversion for MRI susceptibility mapping. https://doi.org/10.1101/278036.

Ravanfar, P., Loi, S.M., Syeda, W.T., Van Rheenen, T.E., Bush, A.I., Desmond, P., Cropley, V.L., Lane, D.J.R., Opazo, C.M., Moffat, B.A., Velakoulis, D., Pantelis, C., 2021. Systematic review: Quantitative susceptibility mapping (QSM) of brain iron profile in neurodegenerative diseases. Frontiers in Neuroscience 15. https://doi.org/10.3389/fnins.2021.618435.

Schenck, C.H., Boeve, B.F., Mahowald, M.W., 2013. Delayed emergence of a parkinsonian disorder or dementia in 81% of older men initially diagnosed with idiopathic rapid eye movement sleep behavior disorder: A 16-year update on a previously reported series. Sleep Medicine 14, 744–748. https://doi.org/10.1016/j.sleep.2012.10.009.

Schenck, C.H., Högl, B., Videnovic, A. (Eds.), 2019. Rapid-Eye-Movement Sleep Behavior Disorder. Springer International Publishing, Cham.

Sethi, S.K., Kisch, S.J., Ghassaban, K., Rajput, A., Rajput, A., Babyn, P.S., Liu, S., Szkup, P., Mark Haacke, E., 2019. iron quantification in parkinson's disease using an age-based threshold on susceptibility maps: the advantage of local versus entire structure iron content measurements. Magnetic Resonance Imaging 55, 145–152. https://doi.org/10.1016/j.mri.2018.10.001.

Sullivan, C., Kaszynski, A., 2019. PyVista: 3D plotting and mesh analysis through a streamlined interface for the visualization toolkit (VTK). J Open Source Softw 4, 1450. https://doi.org/10.21105/joss.01450.

Sun, J., Lai, Z., Ma, J., Gao, L., Chen, M., Chen, J., Fang, J., Fan, Y., Bao, Y., Zhang, D., Chan, P., Yang, Q., Ye, C., Wu, T., Ma, T., 2020. Quantitative evaluation of iron content in idiopathic rapid eye movement sleep behavior disorder. Movement Disorders 35, 478–485. https://doi.org/10.1002/mds.27929.

Takahashi, H., Watanabe, Y., Tanaka, H., Mihara, M., Mochizuki, H., Takahashi, K., Yamamoto, K., Liu, T., Wang, Y., Tomiyama, N., 2018. Comprehensive MRI quantification of the substantia nigra pars compacta in parkinson's disease. European Journal of Radiology 109, 48–56. https://doi.org/10.1016/j.ejrad.2018.06.024.

Thomas, C., Ye, F.Q., Irfanoglu, M.O., Modi, P., Saleem, K.S., Leopold, D.A., Pierpaoli, C., 2014. Anatomical accuracy of brain connections derived from diffusion MRI tractography is inherently limited. Proceedings of the National Academy of Sciences of the United States of America 111, 16574–16579. https://doi.org/10.1073/pnas.1405672111.

Tournier, J.D., Calamante, F., Connelly, A., 2012. MRtrix: Diffusion tractography in crossing fiber regions. International Journal of Imaging Systems and Technology 22, 53–66. https://doi.org/10.1002/ima.22005.

Tziortzi, A.C., Haber, S.N., Searle, G.E., Tsoumpas, C., Long, C.J., Shotbolt, P., Douaud, G., Jbabdi, S., Behrens, T.E.J., Rabiner, E.A., Jenkinson, M., Gunn, R.N., 2014. Connectivity-based functional analysis of dopamine release in the striatum using diffusion-weighted MRI and positron emission tomography. Cerebral Cortex 24, 1165–1177. https://doi.org/10.1093/cercor/bhs397.

Uchida, Y., Kan, H., Sakurai, K., Arai, N., Kato, D., Kawashima, S., Ueki, Y., Matsukawa, N., 2019. Voxel-based quantitative susceptibility mapping in parkinson's disease with mild cognitive impairment. Movement Disorders 34, 1164–1173. https://doi.org/10.1002/mds.27717.

Uchida, Y., Kan, H., Sakurai, K., Inui, S., Kobayashi, S., Akagawa, Y., Shibuya, K., Ueki, Y., Matsukawa, N., 2020. Magnetic susceptibility associates with dopaminergic deficits and cognition in parkinson's disease. Movement Disorders 35, 1396–1405. https://doi.org/10.1002/mds.28077.

Veraart, J., Novikov, D.S., Christiaens, D., Ades-aron, B., Sijbers, J., Fieremans, E., 2016. Denoising of diffusion MRI using random matrix theory. NeuroImage 142, 394–406. https://doi.org/10.1016/j.neuroimage.2016.08.016.

Walsh, D.O., Gmitro, A.F., Marcellin, M.W., 2000. Adaptive reconstruction of phased array MR imagery. Magnetic Resonance in Medicine 43 (5), 682–690.

Wüllner, U., Kassubek, J., Odin, P., Schwarz, M., Naumann, M., Häck, H.-J., Boroojerdi, B., Reichmann, H., 2010. Transdermal rotigotine for the perioperative management of parkinson's disease. Journal of Neural Transmission (Vienna) 117, 855–859. https://doi.org/10.1007/s00702-010-0425-4.

Yushkevich, P.A., Pluta, J., Wang, H., Wisse, L.E., Das, S., Wolk, D., 2016. Fast automatic segmentation of hippocampal subfields and medial temporal lobe subregions in 3 tesla and 7 tesla MRI. Alzheimer's & Dementia: The Journal of the Alzheimer's Association. 126–127.

Zhang, Xuan, Chai, C., Ghassaban, K., Ye, J., Huang, Y., Zhang, T., Wu, W., Zhu, J., Zhang, Xianchang, Haacke, E.M., Wang, Z., Xue, R., Xia, S., 2021. Assessing brain iron and volume of subcortical nuclei in idiopathic rapid eye movement sleep behavior disorder. Sleep 44. https://doi.org/10.1093/sleep/zsab131.